Intrusion-Related Gold Deposits: new insights from gravity and hydrothermal integrated 3D modeling applied to the Tighza gold mineralization (Central Morocco)

Khalifa Eldursi, Yannick Branquet, Laurent Guillou-Frottier, Guillaume Martelet, Philippe Calcagno

Accepted Manuscript

Intrusion-Related Gold Deposits: new insights from gravity and hydrothermal integrated 3D modeling applied to the Tighza gold mineralization (Central Morocco)

Khalifa Eldursi, Yannick Branquet, Laurent Guillou-Frottier, Guillaume Martelet, Philippe Calcagno

PII:	S1464-343X(18)30019-0
DOI:	10.1016/j.jafrearsci.2018.01.011
Reference:	AES 3125
To appear in:	*Journal of African Earth Sciences*
Received Date:	15 July 2017
Revised Date:	16 January 2018
Accepted Date:	18 January 2018

Please cite this article as: Khalifa Eldursi, Yannick Branquet, Laurent Guillou-Frottier, Guillaume Martelet, Philippe Calcagno, Intrusion-Related Gold Deposits: new insights from gravity and hydrothermal integrated 3D modeling applied to the Tighza gold mineralization (Central Morocco), *Journal of African Earth Sciences* (2018), doi: 10.1016/j.jafrearsci.2018.01.011

Intrusion-Related Gold Deposits: new insights from gravity and hydrothermal integrated 3D modeling applied to the Tighza gold mineralization (Central Morocco)

Khalifa Eldursi [a,*,(1)], Yannick Branquet[a,b,c], Laurent Guillou-Frottier[c], Guillaume Martelet[c], Philippe Calcagno[c]

[a] Université d'Orléans, ISTO, UMR 7327, 1A rue de la Férollerie, 45071 Orléans, Cedex 2, France

[b] CNRS/INSU, ISTO, UMR 7327, 45071 Orléans, France

[c] BRGM, ISTO, UMR 7327, 3 av. Claude Guillemin, BP 36009, 45060 Orléans, Cedex 2, France

* Corresponding author: Khalifa Eldursi

eldursik@uregina.ca

Phone: +1 639-999-7464

Fax: +1 306-585-5433

[(1)] Present address: Department of Geology, University of Regina, 3737 Wascana Parkway, Regina, SK, S4S 0A2, Canada

Abstract

The Tighza (or Jebel Aouam) district is one of the most important polymetallic districts in Morocco. It belongs to the Variscan Belt of Central Meseta, and includes W-Au, Pb-Zn-Ag, and Sb-Ba mineralization types that are spatially related to late-Carboniferous granitic stocks. One of the proposed hypotheses suggests that these granitic stocks are connected to a large intrusive body lying beneath them and that W-Au mineralization is directly related to this magmatism during a 287-285 Ma time span. A more recent model argues for a disconnection between the older barren outcropping magmatic stocks and a younger hidden magmatic complex responsible for the W-Au mineralization. Independently of the magmatic scenario, the W-Au mineralization is consensually recognized as of intrusion-related gold deposit (IRGD) type, W-rich. In addition to discrepancies between magmatic sceneries, the IRGD model does not account for published older age corresponding to a high-temperature hydrothermal event at ca. 291 Ma. Our study is based on gravity data inversion and hydro-thermal modeling, and aims to test this model of IRGD and its related magmatic geometries, with respect to subsurface geometries, favorable physical conditions for deposition and time record of hydrothermal processes. Combined inversion of geology and gravity data suggests that an intrusive body is rooted mainly at the Tighza fault in the north and that it spreads horizontally toward the south during a trans-tensional event (D2). Based on the numerical results, two types of mineralization can be distinguished: 1) the “Pre-Main” type appears during the emplacement of the magmatic body, and 2) the “Main” type appears during magma crystallization and the cooling phase. The time-lag between the two mineralization types depends on the cooling rate of magma. Although our numerical model of thermally-driven fluid flow around the Tighza pluton is simplified, as it does not take into account the chemical and deformation contributions, it provides evidence for abandoning the time-lag as an argument for invalidating the existence of a genetic link between older mineralizations and/or hydrothermal events spatially related to younger parent plutons.

Keywords: Jebel Aouam, intrusion-related gold deposits, hydrothermal fluid flow, 3D geological and gravity modeling, combined inversion, rock alteration index

1. Introduction

Intrusion-Related Gold Deposits (IRGD) form a major class of ore deposits, including various deposit styles as diverse as skarns, mineralized breccias, sheeted veins, and disseminations within or peripheral to the intrusion (Thompson et al. 1999; Baker and Lang 2001; Lang and Baker 2001; Hart 2005). They form a distinct class from gold-rich porphyry deposits (Sillitoe 2000) because: i) they are associated with moderately oxidized to reduced small intrusions (hence the name "Reduced Intrusion-Related Gold Deposits" preferred by some authors, such as Hart 2007) which may be emplaced at depths down to 8 km; ii) the metal association mostly includes tin, tungsten, molybdenum, bismuth, tellurium, and arsenic, rather than copper and silver; iii) the sulfide mineral content is low in veins; and iv) the hydrothermal fluids are CO_2-rich. The IRGD mineralization is located within the intrusion and/or its fractured thermal aureole. The intrusions are weakly deformed as they postdate regional ductile shearing and peak metamorphism. The exposed intrusions form one to two kilometer-wide stocks which may correspond to apices or cupolas of an underlying larger plutonic body.

IRGD are generally assumed to be genetically linked to, and coeval with, the emplacement and cooling of these felsic intrusions (e.g. Baker and Lang 2001; Gloaguen et al. 2014). However, little is known about the 3D geometry of the magmatic plumbing system at depth, although it is well-known that pluton morphology can have a complex effect on the formation of related mineralization (e.g. White 1981; Carten et al. 1988; Seedorff 1988; Wallace 1991; Guillou-Frottier et al. 2000; Guillou-Frottier and Burov 2003; Eldursi et al. 2009; Gloaguen et al. 2014), with the general mineralization morphology and location being dependent on the morphology/shape of the associated intrusions. Knowledge of the 3D shape of the intrusion is thus crucial in the exploration for mineralized apices or cupolas. In addition, exploration models can be greatly improved if a detailed history of mineralization processes can be obtained. However, little is known about detailed timing of ore deposition during the emplacement-crystallization-cooling cycles of an intrusive. In particular,

during magma emplacement, crystallization, and cooling, several phases of advective processes (e.g. localized convection cells, hot fluid channels) may disturb local isotherms and thus mineral closure temperatures, which makes obtained mineralization ages very difficult to interpret relative to magmatic cooling ages.

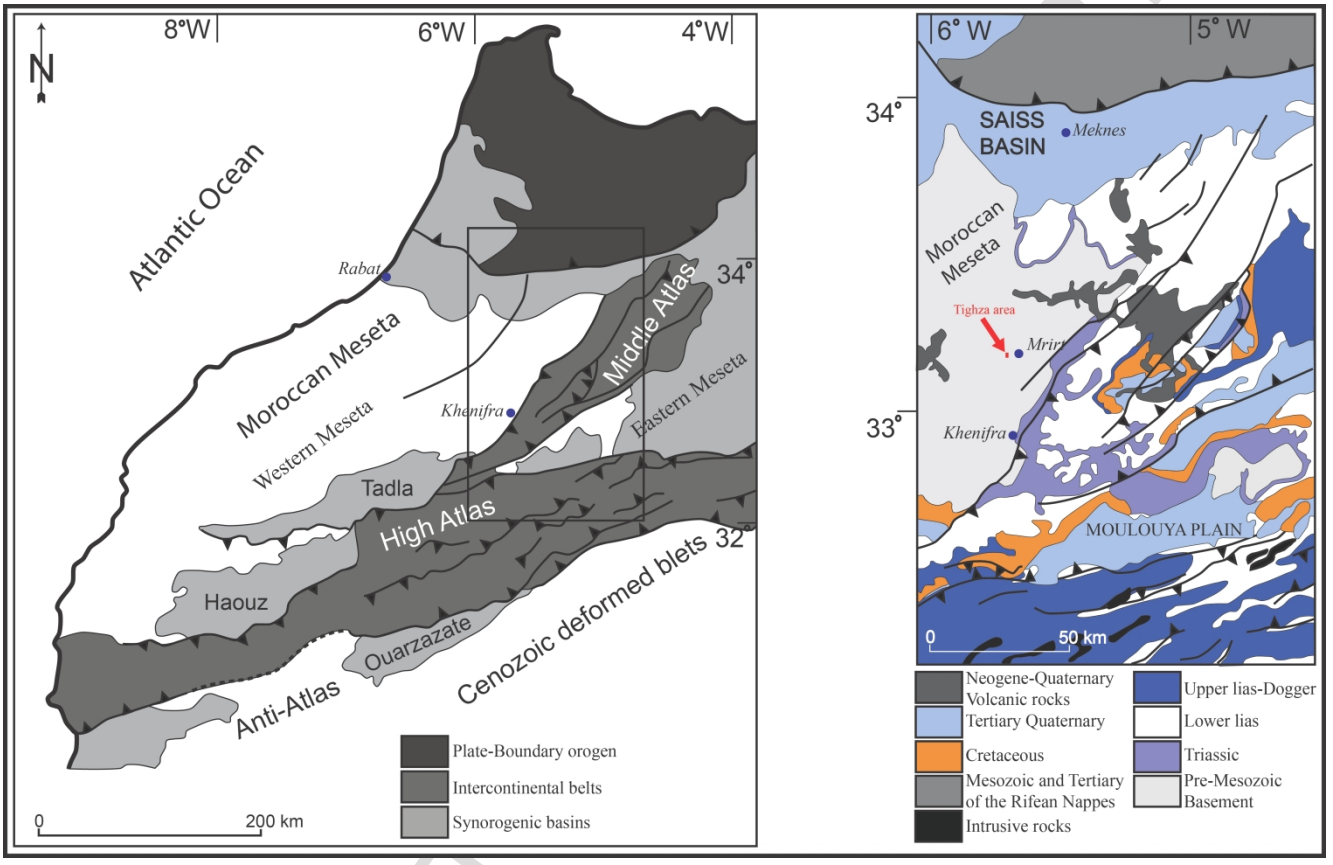

Figure 1 Main geological features of Morocco and location of the Tighza area in the Variscan basement of the eastern Moroccan Meseta (modified after Arboleya et al. 2004).

The Tighza mining district is located in the Moroccan Meseta which is the largest outcrop region of the Variscan Belt rocks in Morocco (Figure 1). It produces 52% of the Pb, 26% of the Ag, and 3.2% of the Zn, of the national production of Morocco at the end of the last century (Wadjinny 1998). The annual production is about 25600 concentrated tones of Pb-Ag, and 4300 concentrated

105 tones of Zn in 2013 (CMT website[2]). The Tighza district contains three main granitic stocks, with
106 other scattered small granitic plugs and dykes (Figure 2). The three main stocks are, from north to
107 south, the Mispickel Granite, Mine granite, and the Kaolin granite. Because these granitic bodies share
108 similar compositional, textural, and mineralogical features, many authors assume that they are part of
109 one single large granitic body at depth to (e.g. Agard et al. 1958; Marcoux et al. 2015).

110 In addition to other economic resources, such as Pb-Zn vein deposits, the area hosts W-Au
111 mineralization with features typical of an IRGD system (Marcoux et al. 2015). This W-Au
112 mineralization and its magmatic context have been extensively studied, particularly dealing with
113 geochronological constraints (Cheilletz and Zimmermann, 1982; Cheilletz, 1984, Watanabe, 2002;
114 Nerci, 2006; Marcoux et al., 2015; Rossi et al., 2016). Even though a general IRGD model is accepted,
115 geochronological data from granitic rocks have led authors to suggest various genetic models for this
116 W-Au mineralization.

117 Two major points will be addressed in this contribution: i) the role of 3D pluton geometry in
118 the mineralization process and localization through 3D gravity data modeling, and ii) the timing of the
119 mineralization, through 3D coupled hydro-thermal numerical simulations. The combination of well-
120 exposed rocks and numerous geochronological data relevant to magma emplacement and associated
121 hydrothermal activities makes the Tighza mining district and its IRGD a particularly suitable candidate
122 for addressing these points.

123

124 **2. The Tighza W-Au mineralization: previous models**

125 **2.1 Geological setting**

126 The Tighza region (or Jebel Aouam region) is located in the Paleozoic Moroccan Meseta,

---

[2] http://www.miniere-touissit.com/cmt-tighza.html

in the eastern part of central Morocco, near the border with the Middle Atlas. It is around thirty kilometers north-west of the town of Khenifra and 7 km west of the city of Mrirt (Figure 1). The region is an area of high to moderate relief (1220 m mean altitude) in the center of which Jbel Aouam (1496 m) emerges. The study area (Figure 2) constitutes a low-grade metamorphic Paleozoic (Ordovician to Visean) series that has been intruded by numerous stocks and dykes. The southeastern portion of the region corresponds to an allochthonous unit that was thrust over a northwestern autochthonous unit (Termier 1936; Ribeyrolles 1972).

After the D1 gravity-driven nappe event (late Visean-Early Namurian, Faïk, 1988), the entire area underwent NE-SW cylindrical folding, resulting from NW-SE horizontal shortening, during the Variscan D2 event (Late Carboniferous - Early Permian, Destreucq, 1974; Marcoux et al., 2015 and references therein). As a result, both bedding planes and weakly developed axial plane cleavages are NE-trending with a dominant steep dip to the NW. The E-W-trending Tighza wrench fault system (Figure 2) is a branch of the regional-scale Aguelmous-Mrirt shear zone (Cheilletz, 1983, 1984). In the study area, it separates a northern from a southern domain. This strike-slip fault has a complex polyphase history. It was first a transtensional right-lateral wrench zone during D2, while the last movements correspond to left-lateral wrenching during a D3 brittle event (Desteucq 1974; Cheilletz 1983, 1984; Marcoux et al. 2015) of Late Permian-Middle Triassic in age (Rossi et al., 2016, 2017).

With the exception of early Carboniferous dolerite sills emplaced during sediment deposition, all magmatic rocks are late to post- Variscan in age. Most of the intrusives belong to an early calc-alkaline magmatic suite and correspond to: i) the three main biotite granite stocks (Mispickel, Mine and Kaolin granites), as well as a small granodioritic stock located in the northeastern part of the study area (Figure 2), and (ii) a well-developed dyke swarm, generally parallel to S0/S1, that are mainly composed of microgranodiorite, microgranite, and aplite (Figure 2). Based on previous studies (Cheilletz 1984; Cheilletz and Isnard 1985; Nerci 2006; Marcoux et al. 2015; Tarrieu, 2014; Rossi et

al. 2016), the four granitic/granodioritic stocks are homogeneous in texture, mineralogy, and geochemistry, suggesting that they are probably derived from a single magmatic source. Other intrusives rocks in the region (not represented in Figure 2) are tholeiitic microdioritic and sparse leucogranitic dykes.

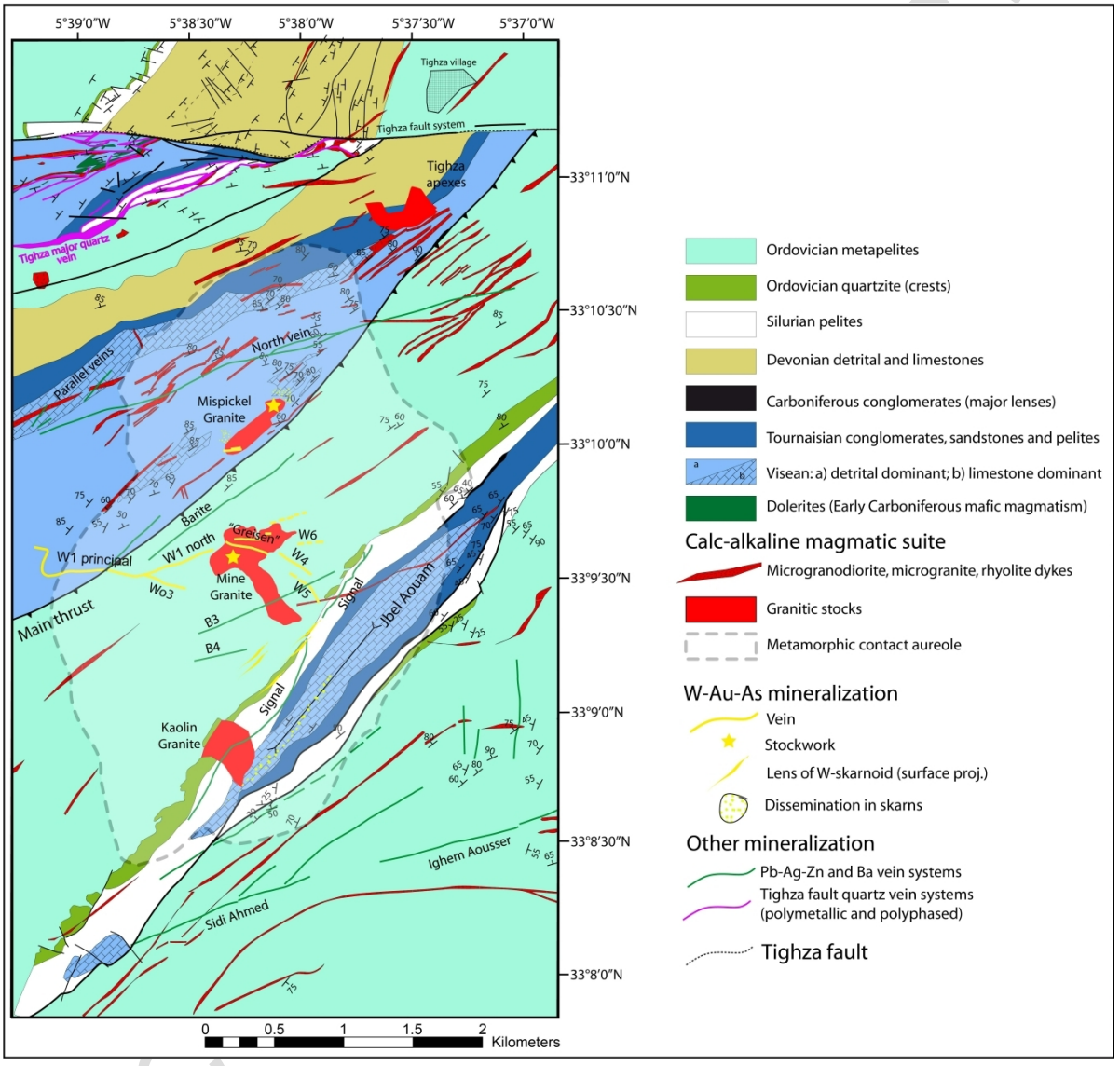

Figure 2 Geological map of the Tighza region compiled from CMT maps and the current field study. The extent of the contact metamorphic aureole is from Cheilletz and Iznard (1985). Only silicic dykes of the calc-alkaline magmatic suite have been represented. W-Au-As mineralization types are from Marcoux et al. (2015).

160 The Tighza region is a polymetallic district containing: i) Pb-Zn-Ag mineralization in thick
161 veins that make the Tighza district the second largest Pb producer in Morocco (Wadjinny 1998;
162 Compagnie Minière de Touissit ("CMT") - Pers. Comm. 2012), ii) W-Au granite-related
163 mineralization (IRGDs), and iii) Ba-Sb vein mineralization. There is a consensus that the Pb-Zn-Ag
164 mineralization formed in epithermal conditions during a late Permian-Triassic magmatic-hydrothermal
165 event disconnected from an older W-Au mineralization (Tarrieu 2014; Cheilletz et al. 2015; Marcoux
166 et al. 2015; Rossi et al. 2016; 2017). Pb-Zn-Ag mineralization developed during the D3 left-lateral
167 wrench event that had a transtensional component. A low-temperature Ba-Sb mineralization in veins is
168 also present in the district ("Barite", B3, B4, and within the Tighza fault quartz vein system; Figure 2).
169 Although no strong evidence has been observed in the Tighza area, based on other neighboring
170 mineralization, the Ba-Sb hydrothermal system is assumed to be older than the Pb-Zn-Ag mineralizing
171 event (Agard et al. 1958).
172 For additional detailed geological data and descriptions concerning the geological setting, refer to
173 Marcoux et al. (2015) and references therein.

174 **2.2 The Tighza W-Au IRGD mineralization: a magmatic-hydrothermal model**

175 The Tighza W-Au mineralization occurs in various styles, such as veins around the Mine granite ("W"
176 in Figure 2), greisen bands crosscutting the Mine granite, stockworks, disseminations in skarns, and
177 lenses of W-rich skarnoids (Figure 2). Three main hydrothermal stages have been proposed (Nerci
178 2006; Marcoux et al. 2015): (i) a primary W-rich skarn stage formed under lithostatic fluid pressure
179 (ca 1.5 kbar) and temperatures up to 580°C, and associated with intrusion of calc-alkaline suite granitic
180 magma, (ii) a second stage responsible for the deposition of Au-As-Bi-Te, and (iii) a third stage that
181 includes base metal (Zn-Cu) mineralization. The three stages occurred during the emplacement-
182 cooling cycle of granitic intrusive activity. The pressure conditions associated with stages 2 and 3 are
183 close to the hydrostatic regime (ca. 550 bars) with temperature around 300°C. Stages 1 and 2 are

184 characterized by CO_2-rich and saline aqueous fluids expulsed from the granitic magma. Structurally,
185 the emplacements of the granitic intrusions and the mineralized veins were controlled and coeval with
186 the D2 right-lateral transtensional deformation. The W-Au mineralization is spatially associated with
187 the main granitic intrusions (Figure 2), however, W-Au mineralization is also found far from the four
188 outcropping granitic stocks (Figure 2). This spatial relationship suggests that the mineralizing system
189 is not restricted only to the close vicinity of outcropping stocks and dykes. In addition, Cheilletz and
190 Isnard (1985) identified a hydrothermal metamorphic aureole, centered on the Mine/Mispickel/Kaolin
191 granitic stocks, that encompasses the W-Au occurrences (dashed contour in Figure 2). As the extent of
192 this metamorphic aureole is large relative to the outcrop extent of the granitic stocks and dykes, the
193 presence of a larger plutonic body, hidden at depth, was proposed. This hypothesis has been recently
194 re-proposed by Marcoux et al. (2015) and Rossi et al. (2016, 2017). Because of this relationship to the
195 igneous intrusive bodies, igneous geochemistry, and the origin/nature of the associated fluids, a model
196 of Intrusion-Related Gold Deposits (IRGD) has been proposed for the Tighza W-Au mineralization
197 (Marcoux et al. 2015). Subtle distinctions led Rossi et al. (2016, 2017) to classify this W-Au
198 mineralization as "porphyry-style", a deposit group that includes and/or overlaps the IRGD definition
199 according to different authors and classifications.

200 The main difference between the various Tighza W-Au metallogenetic models is the age of the
201 granitic magmatism associated with the mineralization. K/Ar and Ar/Ar dating on biotite and
202 muscovite from the W-Au hydrothermal materials yields a coherent and unique age of ca. 285 Ma
203 (Cheilletz 1984; Nerci 2006, Marcoux et al. 2015). Only one Ar/Ar age (291.8 ± 0.3 Ma), from a
204 sample of phlogopite associated with quartz from the W1 north veins (Figure 2), suggests the
205 possibility of an earlier phase of high-temperature hydrothermal deposition (Marcoux et al. 2015). In
206 this sample, no ore mineral is directly associated with the phlogopite, however, the quartz and
207 phlogopite assemblage is the classical gangue material to the Tighza W ore. This suggests that the

earlier high-temperature hydrothermal event indicated by this age date might not be barren. The significance of this older age and the timing of this hydrothermal event will be discussed later in the paper.

In contrast, radiometric ages obtained for the granitic magmatism are more widely distributed. The K/Ar and Ar/Ar ages of igneous micas from the Mine, Kaolin, and Mispickel granitic stocks cluster around 286 Ma (Cheilletz 1984; Watanabe 2002; Nerci 2006; Marcoux et al. 2015), but U-Th/Pb zircon intercept ages yield 309 ± 10 Ma for the Mine granite and 295 ± 9 Ma for the Kaolin granite (Rossi et al. 2016). Based on these ages, Rossi et al (2016, 2017) proposed that the outcropping granitic stocks of the Tighza area (Figure 2) were emplaced during an old magmatic event (between 320 and 300 Ma), and thus they could not be responsible for the W-Au hydrothermal event and are disconnected from the IRGD genetic model. This hydrothermal event would then be related to a younger hidden laccolith emplaced between 300 and 280 Ma with a large associated hydrothermal contact metamorphic halo. The Rossi et al. (2016, 2017) model thus implies the non-coeval intrusion of at least two plutonic complexes at depth. Alternatively, Marcoux et al. (2015) proposed that the W-Au mineralization is genetically related to the emplacement of the outcropping granitic stocks, with the stocks being interpreted to be plutonic apices (cupolas) related to a single underlying batholith (e.g. the Yerrington batholith in Nevada, USA, which has several apices that are separated by ~1-2 km; Dilles and Profett 1995).

3. Coupled gravity and geological study

Modeling of gravity data has long provided information valuable in defining pluton shapes at depth, pluton thickness variations, and locations of possible root zones. In addition, gravity and 3D geological models aid in understanding pluton emplacement mechanisms, regional kinematics, and strain fields (e.g. Vigneresse 1990; Lyons et al. 1996; Martelet et al. 2004; Talbot et al. 2004; Joly et al. 2008; Wei et al. 2016).

3.1 Gravity data acquisition

A detailed gravity survey of the Tighza region was acquired using a grid with minimum average sampling spacing of about 250 m. The survey was supported by: i) a detailed (1:5,000), digital, and georeferenced mining company (CMT) topographic map, ii) a 30 m Digital Elevation Model (DEM) used in areas without available topographic mapping, and iii) a detailed geological map from the CMT improved by new field data collected during this study (Figure 2), and iv) field structural measurements (bedding, faults, fold axes, etc.) as point data in a GIS database. Gravity data from 320 gravity stations were obtained using a Scintrex Model-CG3-M gravimeter. Station altitudes were determined through plotting GPS station location data on the detailed topographic map and the DEM. The gravity data were fully processed to produce the complete Bouguer anomaly, following reduction of gravity earth-tides, instrumental drift, and free air, plateau, and terrain corrections (using three high, intermediate, and low resolution DEMs, following the method of Martelet et al. 2002). We used the Hayford (1930) reference ellipsoid and the Bouguer reduction density was chosen to be 2600 kg/m^3; a value close to the average density of the rocks outcropping in the area. Given the rather gentle topography in the study area, the error due to the terrain corrections is estimated to not exceed 0.2 mGal. Taking into account all other sources of error, in particular the vertical positioning accuracy, the overall accuracy of the dataset is estimated to be around ± 1 mGal. Finally, the data were interpolated onto a 100 m grid using a standard minimum curvature algorithm. As the new gravity survey was not tied to the existing Moroccan gravity station network, these new data cannot be merged into the regional gravity database. At the scale of the study area, no regional trend in the gravity data was observed, therefore the data interpretation and modeling was based on the complete Bouguer anomaly.

3.2 Gravity data results and interpretation

The Bouguer gravity data are presented in Figure 3. Three different ranges of Bouguer anomalies are

present in the region: i) strong negative values (dark blue colours) that correspond, in part, to the outcropping granitic stocks and granitic dyke swarms, while others are likely related to thicker zones of a probable underlying pluton; ii) strong positive values (red colours) that correspond to high-density rocks, which are normally associated with the host Paleozoic sediments; and iii) moderate anomalies (light blue to yellow colours) that are not easily related to a specific outcropping geology.

In the northern part of the study area, the Tighza fault system is clearly recognizable in the gravity data as a sharp E-W-trending gravity contrast corresponding to the contact between a lower-density southern domain and a higher-density northern domain (Figure 3). The southern domain is characterized by numerous and voluminous outcropping lower-density granitic rocks and a large associated contact metamorphic thermal aureole, while very few granitic rocks are found within the northern domain.

From these gravity data, it is reasonable to suggest that a large-scale plutonic complex (referred to herein as the "Tighza pluton") is present at depth, south of the Tighza fault system. Because the Tighza fault system was active during successive D2 and D3 events, it is difficult to identify a potential fault control during the emplacement of the Tighza pluton. However, as the W-series structures controlled the emplacement of the Mine granite apex during D2 (Figure 2; Marcoux et al. 2015), it cannot be ruled out that the Tighza fault may have controlled spatial emplacement of the proposed pluton. In this case, a major feeder zone could be located in the vicinity of the fault, with the magma ascending along the fault and moving southward to form a laccolith (as proposed by Rossi et al. 2017 for their "hidden pluton"). In support of this hypothesis, several gravity lows demarcate the southern side of Tighza fault. In addition, other local strong negative Bouguer anomalies suggest other possible roots or apices, in particular in the eastern and southern parts of the study area. In contrast, the western region is associated with slightly positive anomalies, suggesting few or no granitic intrusives in this area.

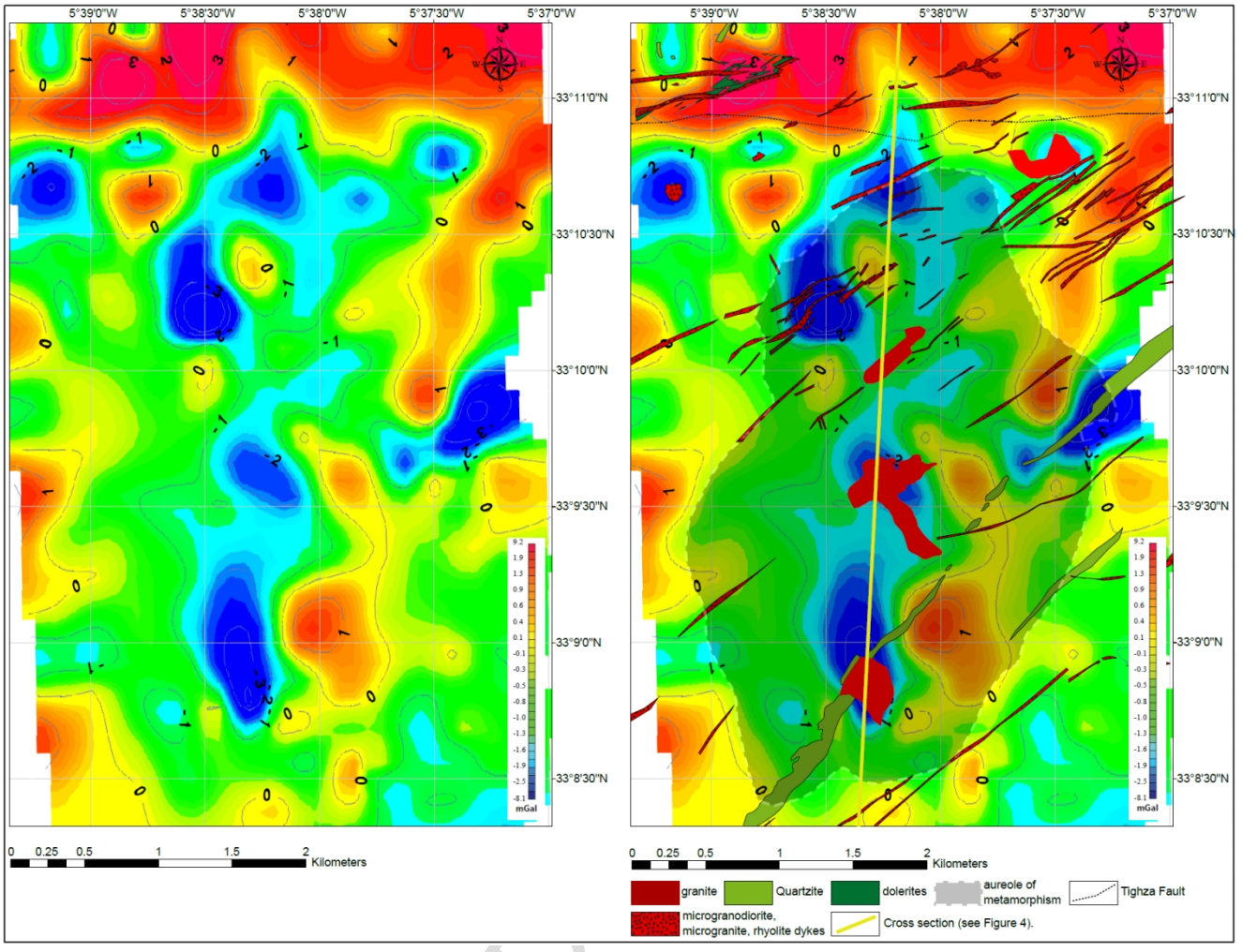

Figure 3. Left: Bouguer anomaly map of the Tighza region. Right: Same map with draping of the main geological features. The Tighza fault system corresponds to a strong contrast between a positive anomaly in the northern domain and a southern domain displaying low to strongly negative anomalies.

3.3 2D Gravity modeling

Mapping of the gravity data alone does not provide accurate constraints on the geometry and thickness of the proposed underlying Tighza pluton. Localized gravity lows suggest the presence of thicker granitic bodies and indistinct low-intermediate values that occupy a large part of the area could attest to the presence of granitic material at depth, south of the Tighza fault. Without field indications

of these suggested features, the hypothesis to be tested was that the localized gravity lows, parts of which correspond to outcropping granitic stocks, could be apices of a batholith lying beneath them (Figure 3). Noteworthy, a multi-phase magmatic history as suggested by Rossi et al. (2016, 2017) cannot be easily depicted by gravity modeling in first order approximation, since gravity data cannot solve time-dependence of magmatic history. Deciphering such complex multi-stage magmatism by gravity modeling would be enhanced by (i) high density contrast between the different magmatic injections; (ii) non-telescoped plutonic complexes with a sufficient thickness of host rocks in between. Since both conditions are not clearly established, the gravity modeling might be inefficient in imaging such complex magmatic scenario.Several 2D cross-sections were modeled to construct the pluton geometry at depth, using the Geosoft GM-SYS software. A cross-section oriented in the NNE-SSW direction, cross-cutting the three outcropping granitic stocks (Mispickel, Mine, and Kaolin granites; Figure 3) is presented in Figure 4. The 2D modeling was constrained by: 1) surface geological and structural data, 2) geometrical constraints derived from indirect interpretation of the measured gravity data, and 3) densities of the lithological units. The subsurface extension of the granitic stocks at depth (geometries) and surrounding rocks were adjusted until the gravity effect of the model reproduced the profile of the field-measured Bouguer gravity data. Despite the non-uniqueness of this solution, the modeled geometry is consistent with the available gravity data. The obtained geometry (Figure 4) suggests that the granitic stocks merge at a shallow depth into a single plutonic body with a thickness ranging between 0.3 and 1 km.

3.4 Coupled gravimetry and geology 3D model

The coupled gravimetry and geology 3D model was built in a georeferenced system and takes into account: i) the digital elevation model (DEM), (ii) surface geological mapping, and (iii) 2D

313 geophysical cross-sections. We used 3D GeoModeller[3] modeling software to integrate the available
314 information, such as geophysical cross-sections and geological observations (lithological and structural
315 measurements), into a common 3D geometrical framework. All these data were jointly used to produce
316 a 3D geostatistical interpolation with resulting 3D geological geometries (Lajaunie et al. 1997;
317 Calcagno et al. 2002; Calcagno et al. 2008).
318

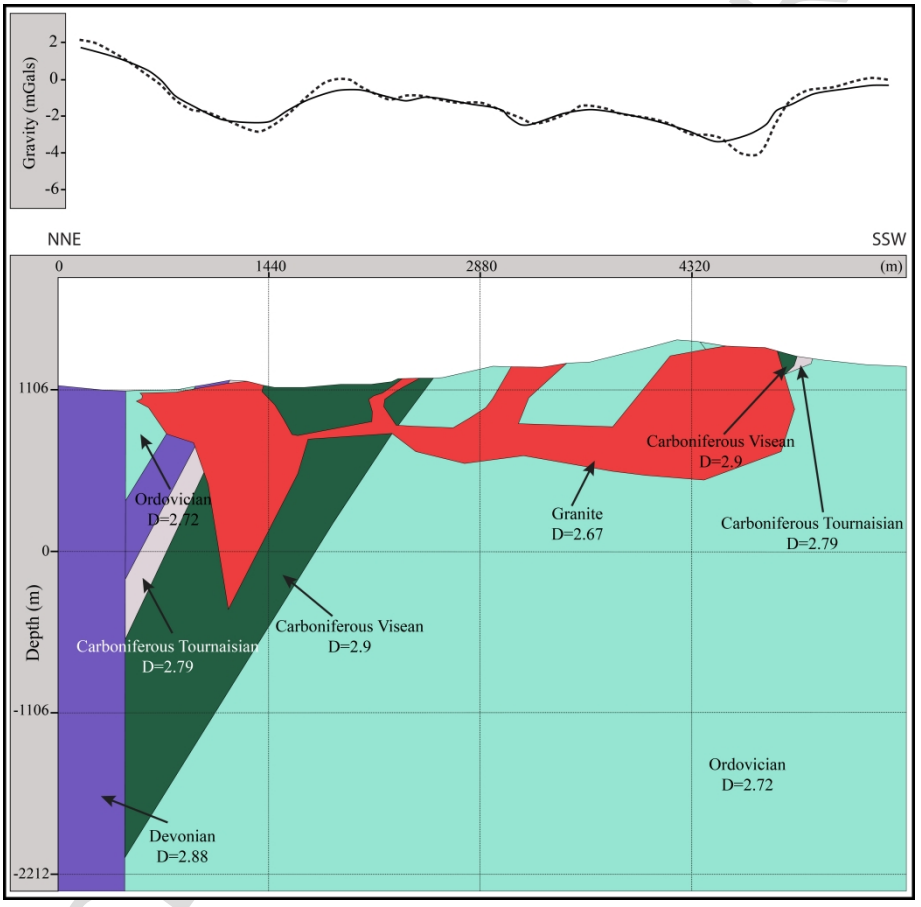

319

320 *Figure 4 Bottom: 2D gravity model of the proposed Tighza pluton; top: gravity effect of the model*
321 *(solid line) fitted to the measured Bouguer anomaly (dotted line). D is the rock density used for*
322 *modeling.*

---

[3] commercial software developed by BRGM and Intrepid Geophysics (Calcagno et al. 2008; Guillen et al. 2008); http://www.geomodeller.com

323 The initial 3D model of the proposed Tighza pluton was constructed using a maximum depth
324 around 1 km and one face of the model was fixed at the major Tighza fault. These constraints were
325 based mainly on the 2D cross-sections (e.g. Figure 4). Another constraint was the assumption that the
326 intruded body is thicker at field-identified apices (e.g. Mispikel, Mine, and Kaolin granites) and in
327 other places where the Bouguer gravity map displays strongly negative values (Figures 3, 4). The
328 initial geometry was interpolated in 3D based on eight cross-sections, as well as the surface geology
329 and topography. Intersections between cross-sections, geological boundaries, and structural features
330 were extrapolated with apparent dip. In order to make the 3D model consistent with all of the 2D
331 information, the 3D model was slightly adjusted manually where necessary, taking into account field
332 geological observations and using 2D balancing techniques. When a realistic 3D model was achieved,
333 satisfying all available data/information, it was discretized into a 3D matrix of voxels, prior to further
334 refinement in a 3D gravity inversion. This last stage of 3D discretization is necessary to ensure that all
335 complex 3D effects of the geological features are correctly taken into account and that the 3D
336 interpolation has not produced any unexpected deformation of these features.
337 In the stochastic 3D gravity inversion, implemented in 3D GeoModeller, the initial 3D geometrical
338 model is randomly modified voxel by voxel over millions of iterations (Guillen et al. 2008), with the
339 gravity effect being recomputed at each step and compared to the measured gravity map. The Monte
340 Carlo exploration of model space ensures that the "data minus model" misfit decreases during the
341 course of the iterations until an acceptable difference between the model effect and the measured data
342 is attained. For the Tighza gravity inversion, the threshold of misfit was fixed at 1 mGal, which is the
343 estimated accuracy of the Bouguer anomaly data.
344 This means that all the 3D models tested during the inversion process that had a Root Mean Square
345 (RMS) misfit lower than 1 mGal were considered as "valid 3D geometrical gravity models". 2 million
346 iterations were run and more than 1.1 million models were thus defined as "valid". Then, these 1.1

347 million models were statistically analyzed to obtain the "most probable density model" which is
348 inferred by allocating to each voxel the density with the maximum probability computed from all the
349 "valid density models".

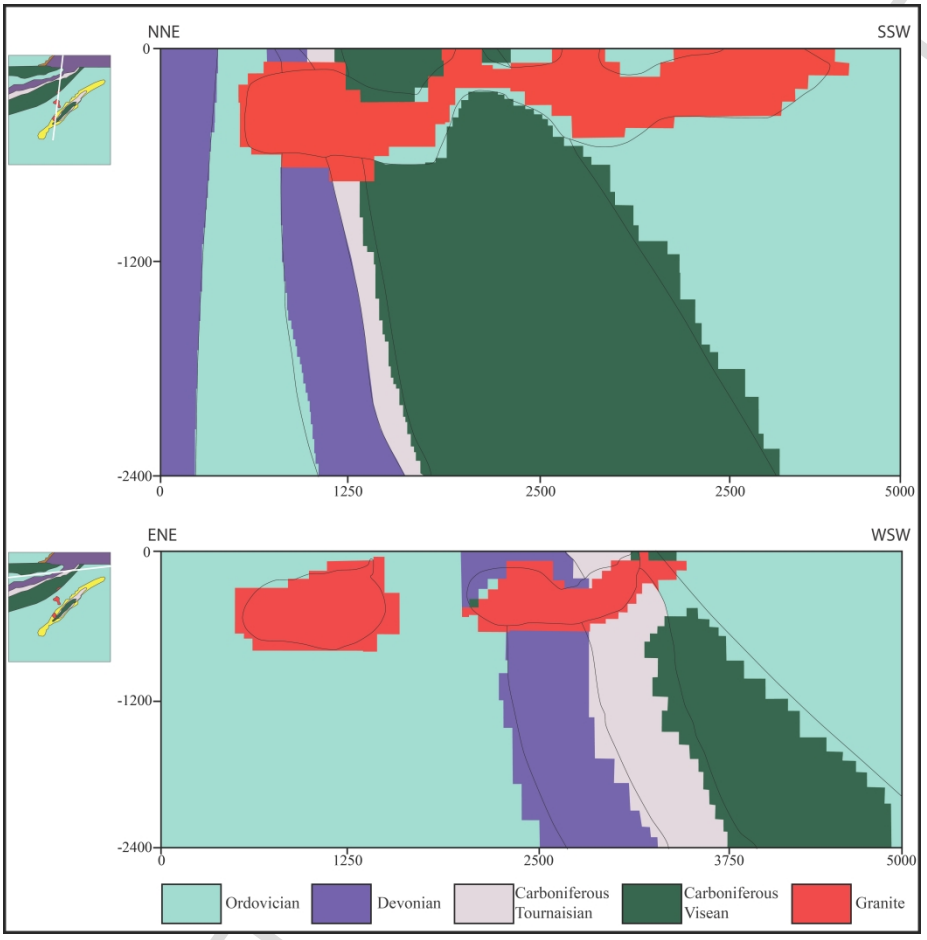

350

351 *Figure 5 N-S (a) and NE-SW (b) cross-sections displaying the result of the 3D gravity inversion in*
352 *terms of the most probable lithology. The black solid lines represent the starting geological model.*

353

354 The same can be done regarding lithology. This is illustrated in Figure 5 along two cross-
355 sections for which each pixel of the cross-sections was queried in terms of most probable lithology.
356 These two cross-sections show that the most probable locations of the geological bodies, as derived
357 from the gravity inversion, is globally close to the 3D geological starting model (represented by black
358 lines in Figure 5). This confirms the overall good quality of the 2D gravity models used to constrain

359 the initial 3D geological model. Thus, by construction, the geometries of the 3D inverted model are in
360 good accordance with the gravity data (with a RMS misfit lower than 1 mGal over the entire study
361 area). Figure 6 displays the final 3D model of the Tighza area, including the resulting gravity
362 inversion.
363

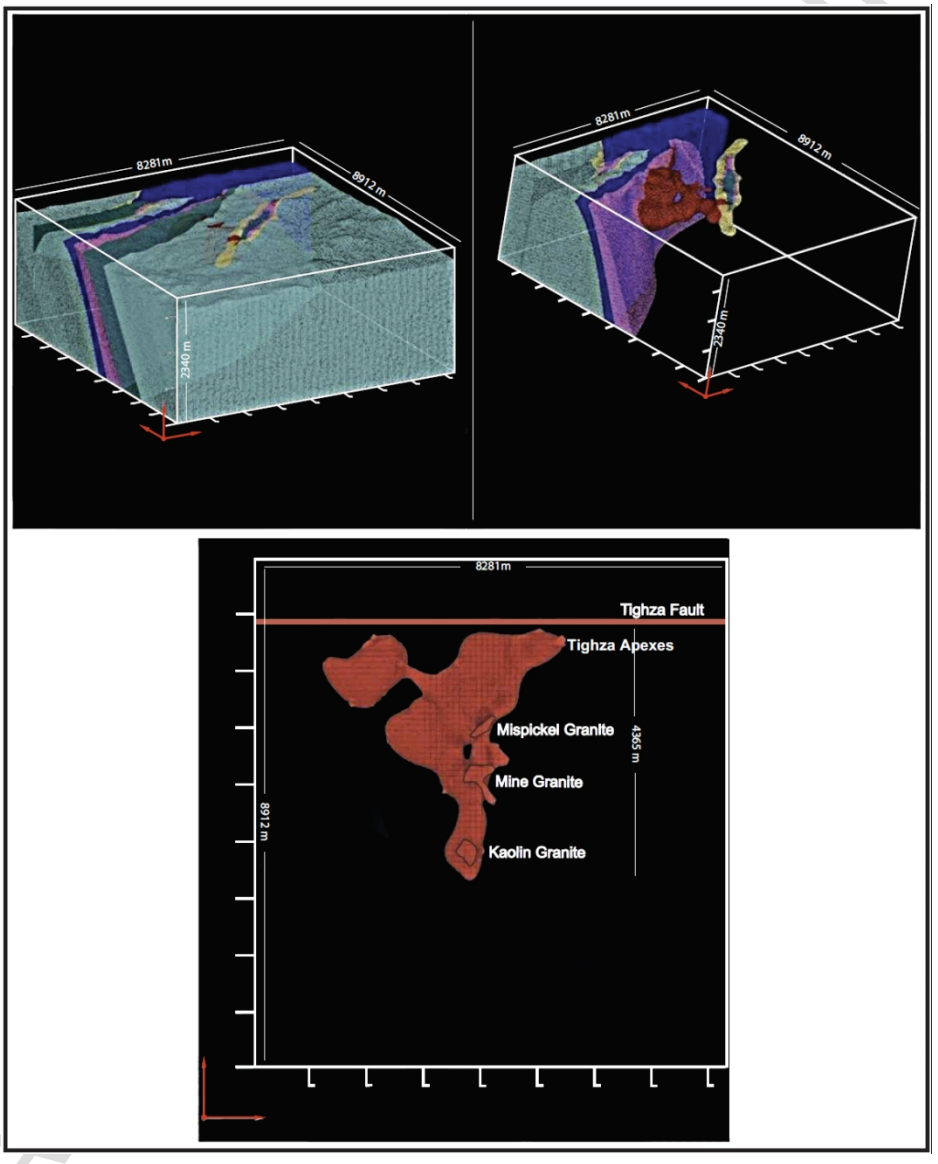

364

365 *Figure 6 At the top, two snapshots of the final 3D model of the area based on geology and gravity*
366 *combined inversion. At the bottom, the most probable 3D architecture of the Tighza pluton in plan*
367 *view.*

4. 3D numerical hydrothermal modeling

4.1 Hydrothermal coupling and numerical modeling construction

In a previous study (Eldursi et al. 2009), 2D numerical modeling of fluid circulation around granitic bodies was performed and applied to various natural cases, some of them including the presence of plutonic apices or proximity to a low-angle normal fault. Here, a similar numerical modeling is focused on the proposed Tighza plutonic system.

Firstly, for this numerical investigation, we chose the best 3D geometry obtained from gravity modeling: three apexes connected at depth to a laccolithic intrusion as represented in the Tighza IRGD model of Marcoux et al. (2015). However, the 3D intrusion geometry was simplified because using a complex 3D geometry for the pluton would not be useful, as thermal diffusion tends to smooth out small-scale asperities. The simplified geometry chosen was a box-like shape with dimensions of 4000x1200x500 m^3, corresponding to a large-scale batholith, surmounted by three apices with unique dimensions of 500x500x1000 m^3 (Figure 7). The main granitic stocks were emplaced at a depth of circa 5500 m, based on fluid inclusion analyses (see model of Marcoux et al. 2015, with lithostatic fluid pressure during the stage "W").

Following this simplification approach, only the W1 structure was chosen to be included in the model due to its economic importance (Figure 2). It was represented as a permeable fracture with a vertical box-shape (200 m wide and 1000 m long) located next to the middle apex that represents the Mine granite (Figure 7). Moreover, to simulate the effects of permeable fracture zones during W-Au hydrothermal event, the "W" veins network (Figure 2) were considered to be important and were simplified as a high-permeability zone in the west-east direction. These simplifications aim at enhancing first-order controlling physical processes associated with both the presence of plutonic apices and of a permeable zone (e.g. fractures/fault).

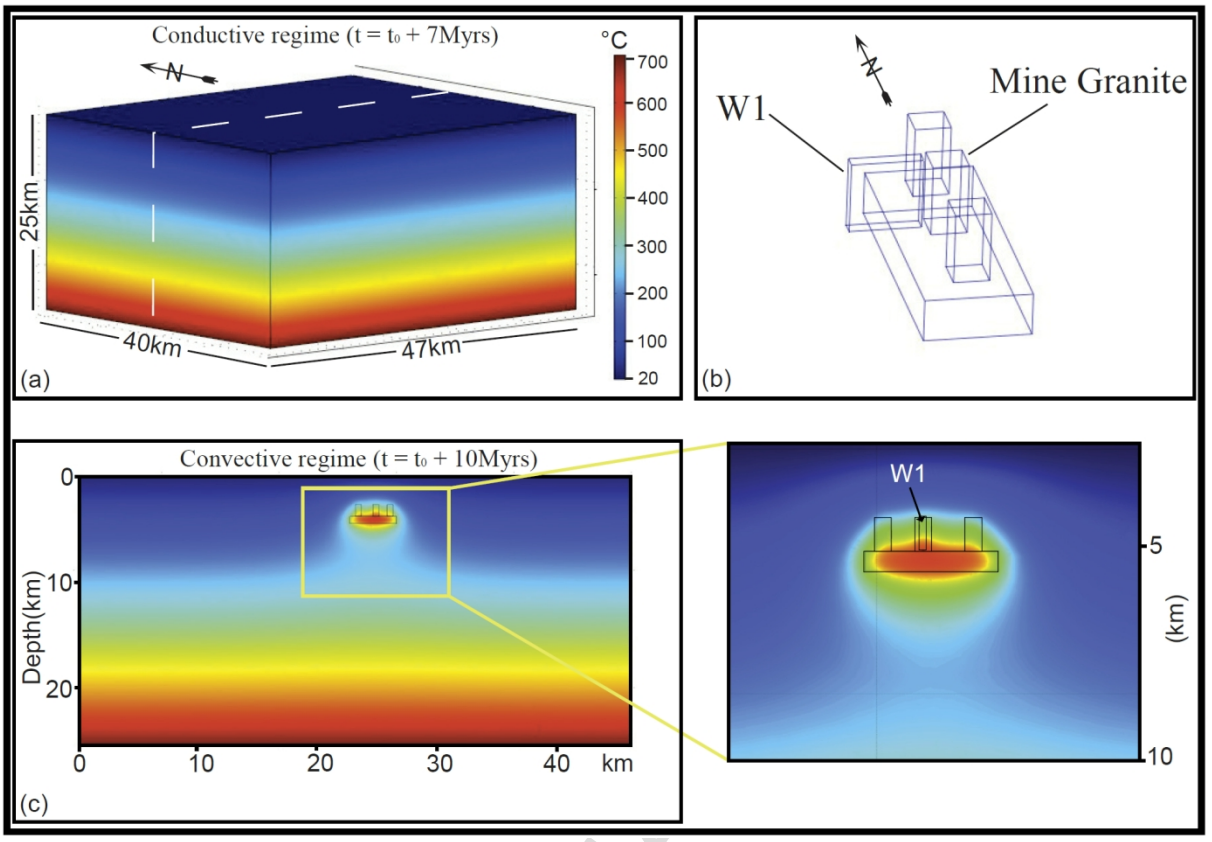

392

393 *Figure 7 Simplified 3D hydrothermal model of the Tighza region: a) the thermal steady-state of the*
394 *whole model at time t_0+7 Myrs, b) the simplified 3D model geometry of the Tighza pluton and the W1*
395 *structure, c) enlarged view of the hottest phase of emplacement (t_0+10 Myrs.). Colored scale is in (C°),*
396 *from 20 to 750°C.*

397

398 As for the previous 2D models of Eldursi et al. (2009), heat transfer in a porous medium was
399 coupled with Darcy law, and mass conservation is applied. The basic numerical scheme was tested and
400 validated by reproduction of different benchmark tests (Gerdes et al. 1998; Rabinowicz et al. 1998;
401 McKenna and Blackwell 2004). Permeability was considered to be depth-dependent, and fluid density
402 and viscosity were considered to be temperature-dependent. All governing equations, physical laws,
403 boundary conditions, and initial thermal and fluid flow regimes are detailed in the Appendix.

404 The 3D hydrothermal modelling of the proposed Tighza pluton includes three phases, 1) a first

phase (from 0 to 7 Myrs) designed to reach thermal equilibrium (thermal steady-state before triggering the second phase); 2) a second phase during which the pluton temperature was increased regularly up to its emplacement temperature (700°C) for a duration of 3 Myrs (7 to 10 Myrs; Figure 8; details presented in Eldursi et al. 2009), and 3) a third phase from 10 to 20 Myrs, during which the granitic body was considered as a fully crystallized felsic body, cooling with time, and where petrophysical parameters (such as thermal conductivity, heat capacity, and density) varied continuously with temperature (Eldursi et al. 2009). The fault permeability followed a depth-dependent function during the first phase (see Appendix), and was set to 10^{-15} m² during the second and third phases. The host rock permeability followed a depth-dependent function during the three phases.

4.2 Rock alteration index

During the computation of the numerical model, temperature and velocity fields are recorded, and a Rock Alteration Index (RAI) is computed as the scalar product of fluid velocity and temperature gradient:

$$RAI = \vec{u} \cdot \vec{\nabla} T \quad (1)$$

RAI is a physical index defined by Phillips (1991) and used in several studies (e.g. Zhao et al. 1998; Raffensberger and Vlassopoulos 1999; Harcouët-Menou et al. 2009). It is designed to represent a local cooling rate such that when the RAI value is negative, mineral precipitation occurs. When the RAI value is positive, i.e. when the fluid flows towards higher temperatures, mineral dissolution occurs. To account for the highest cooling rates, negative values can only be retained with fluid velocity exceeding 10^{-10} m.s^{-1}. To do this, a binary scalar, the "restricted-RAI" (referred to herein as R²AI), is set to 1. For other negative RAI values (i.e. with a velocity lower than 10^{-10} m.s^{-1}) and for positive values of the RAI, R²AI is set to 0. Consequently, patterns of R²AI illustrate at a given time the location of the most probable zones of mineralization. The use of this "restricted-Rock Alteration Index R²AI" in a previous study on 2D numerical modeling of fluid circulation around granitic bodies

(Eldursi et al. 2009) led to the prediction of favorable mineralized zones for different natural cases.

4.3 Results of mineralization patterns

The history of probable zones of mineralization (PZM) obtained by applying the R^2AI factor during the emplacement phase (Phase 2; 7-10 Myrs) and the cooling phase (Phase 3; 10-20 Myrs) is displayed in Figure 8:

1) The first appearance of a PZM occurred, at the bottom of W1, during the first 0.2 Myr. of emplacement (7.2 Myrs; Figure 8a);

2) After 0.3 Myr of emplacement, the PZM extends laterally along the margin of the magmatic body and upward into the permeable fault (7.3 Myrs; Figure 8b);

3) The PZM continues to cover all of the margins of the magmatic body and rises up into the permeable zone (W1 structure) after 1.8 Myrs (8.8 Myrs; Figures 8c-8e).

4) As the temperature increases due to magma emplacement, the PZM extends and covers the top of the middle apex after 2.4 Myrs (9.4 Myrs; Figure 8f).

5) At the hottest phase of emplacement, the PZM covers almost the entire intruded body and fills up the permeable zone (10 Myrs; Figure 8g).

6) During the cooling phase, the PZM concentrates along the western and eastern margins of the intruded body, and inside the permeable zone during the first 0.02 Myr of cooling (10.02 Myrs; Figure 8h).

7) After 0.06 Myr of cooling, the PZM is restricted to the bottom part of the permeable zone only (10.06 Myrs; Figure 8i).

Noteworthy, the use of R^2AI coupled with W-Au temperature deposition range determined in Marcoux et al. (2015) has been tested in order to optimize the PZM: as a result, the numerical PZM remain unchanged comparatively to ones obtained with R2AI only. Using these results, the numerically modeled time for where the PMZ best matches the observed mineralization

453 pattern at Tighza was determined.

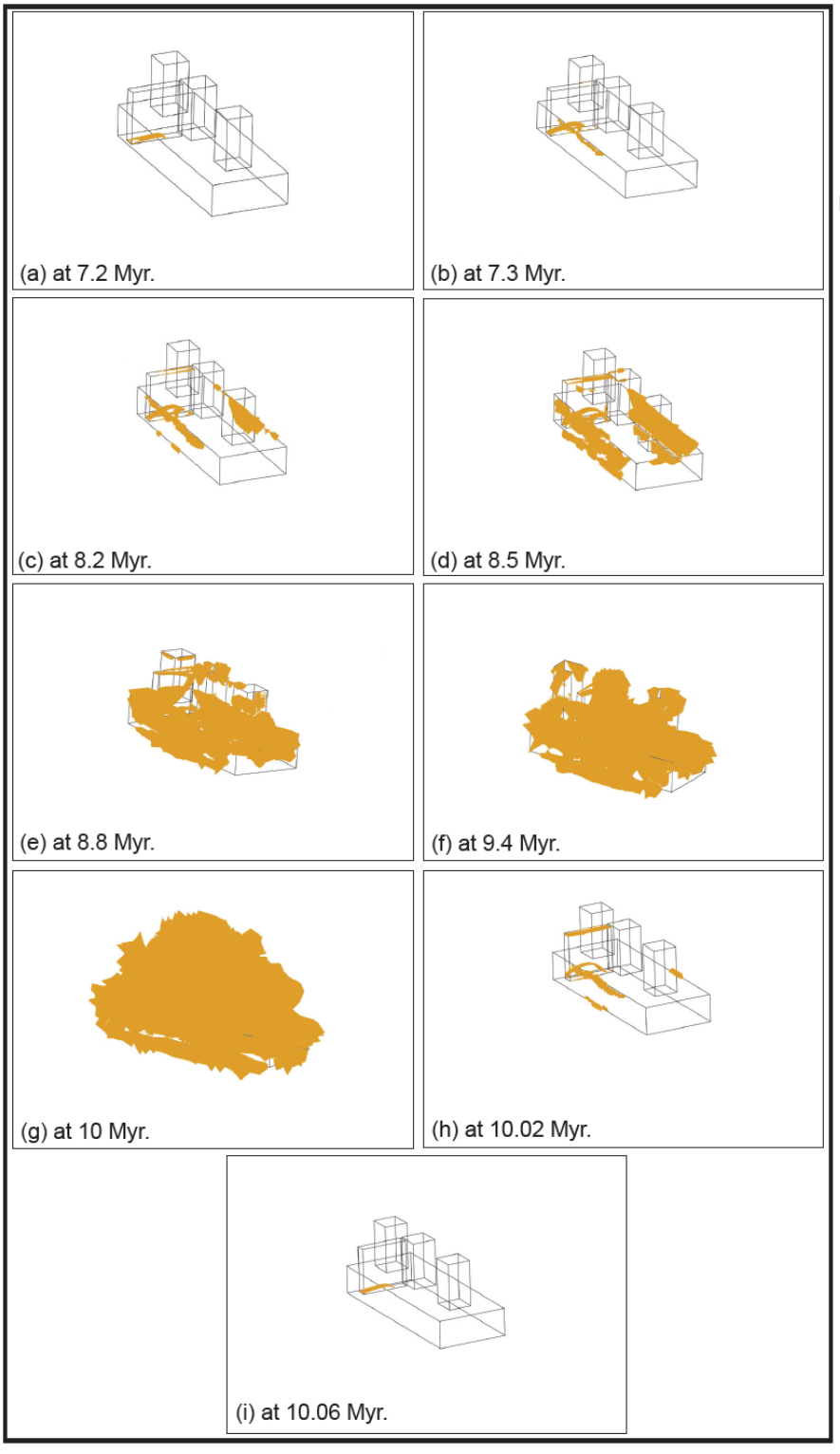

454

455 *Figure 8 Evolution of R^2AI during the emplacement and cooling phases, the colored zone shows the*

456 *most probable zones for mineralization (Eldursi et al. 2009).*

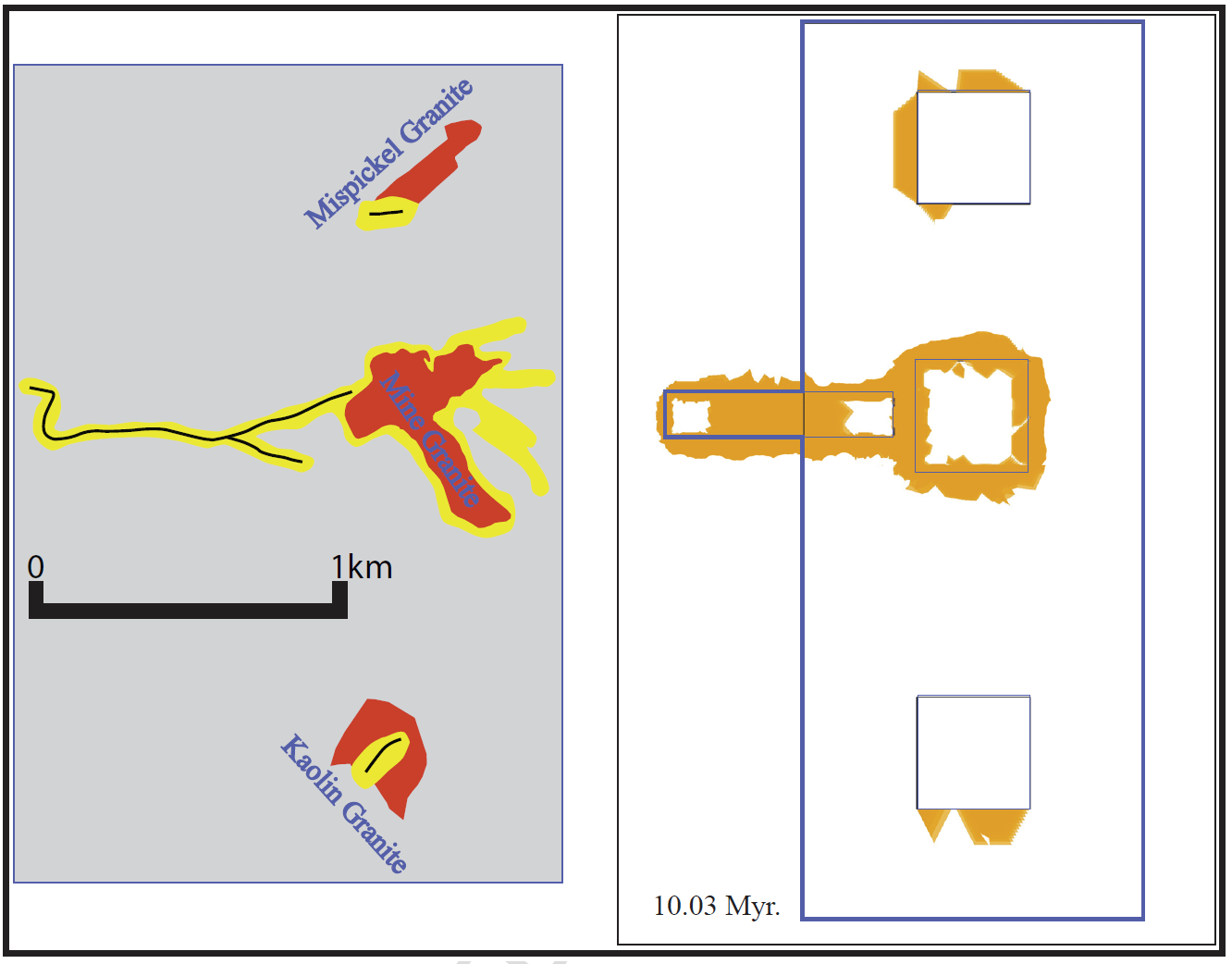

Figure 9 Plan view of mineralized areas (yellow) as observed in the field (left), and (orange) inferred from the numerical model at time t_0+10.03 Myrs (right, at a depth of 4700 m).

Figure 9 presents in plan-view a map of the simplified distribution pattern of the Tighza W-Au mineralization against numerically–inferred PZM determined for 0.03 Myr after the hottest phase (10.03 Myrs) at a depth of 4700 km. At this time, the, PMZ best matches the observed Tighza W-Au distribution pattern. Thus, the observed mineralization pattern, which is characteristic of the "Main" type of mineralization, occurs in the model shortly after the hottest phase of pluton emplacement (10 Myrs, when the pluton produces the maximum heat energy), but it does not continue for long time, as the PZM disappears after 0.06 Myr of cooling (10.06 Myrs; Figure 8i).

Thus, there is a probability of "Pre-Main" mineralization that is modeled from 2.8 Myrs before

468 the hottest phase and extends more and more up to the hottest part of the emplacement at 10.0 Myrs.
469 When the pluton has completely cooled, the thermal regime returns to equilibrium as it was before the
470 emplacement and no evidence of favorable physical conditions for mineralization are observed in this
471 period.

472 **5. Discussion**

473 **5.1 Coupling 3D geological modeling and gravimetry of the Tighza pluton**

474 To build a realistic 3D model of proposed Tighza pluton, geological field data like structural
475 orientations, petrophysical measurements of different geological units, and geophysical data (gravity)
476 were integrated. The sharp contact between the positive Bouguer gravity anomalies in the north and
477 the moderate to low negative anomalies to the south reflects essentially the contact between high-
478 density host rocks and low-density intrusives, respectively, that exactly traces the Tighza fault. This
479 relationship is compatible with a model in which the proposed Tighza syntectonic pluton was rooted in
480 the Tighza fault and spread toward the south as a horizontal sheet during D2 at which time the Tighza
481 fault acted as a right-lateral oblique slip normal fault. However, to account for the D3 event, which
482 may have cut off the northern edge of the laccolith, additional arguments must be provided to confirm
483 the syntectonic nature of this pluton.

484 The results of the gravity data interpretation resulted in the definition of three different
485 categories: 1) high positive anomalies that correspond to the material composed mainly of
486 metasedimentary mica schist, 2) low negative anomalies that correspond to granitic stocks and dykes,
487 and 3) moderate negative anomalies that were modeled as a sub-horizontal magmatic sheet located
488 beneath the granitic stocks. These geophysical and geological features suggest the presence of a single
489 batholith-shaped pluton at depth associated with granitic cupolas/apices at surface. As expected, the
490 best 3D solution obtained does not allow us to depict a deeper intrusion separated from a shallower
491 intrusion by host rock panels as drawn in Rossi et al. (2017). However, this does not mean that this

two-intrusions scenario is wrong (e.g. telescoping etc…). Noteworthy, a single intrusion at depth does not preclude a long-lived pluton construction with various "pulses" of magma inputs at different times.

5.2 Timing of mineralization events and thermo-chronological constraints

The results of the modeling allow apparent radiometric age discrepancies in such magmatic-hydrothermal systems to be highlighted. Indeed, the presence of an early high-temperature hydrothermal event (EHE, potentially economic; see above) has been demonstrated and dated at 291 ±0.3 Ma on phlogopite (Marcoux et al. 2015, see their initial stage on Figure 15A). This EHE developed within the W1 north vein close to the Mine granite which yields very homogenous Ar/Ar ages on micas of around 286 Ma. Because the EHE and the major hydrothermal event leading to the "Main" type W-Au deposition are both clearly related to magmatic activity, the presence of a difference for the two mineralization types in the ages obtained using the same radiometric method is consistent with the modeling results. The 3D hydrothermal models provide a possible answer for this difference. Indeed, in the numerical model we assumed a magmatic emplacement period lasting 3 Myrs (from 7 to 10 Myrs; with the ultimate hottest phase at 10 Myrs) that is reasonable for a long-living emplacement period (e.g. Annen et al. 2006). At Tighza, this hypothesis is coherent with the long-lasting 295-280 Ma magmatic-hydrothermal event responsible for the W-Au mineralization and related (hidden) granite intrusion proposed by Rossi et al. (2016, 2017). The application of R^2AI in the Tighza 3D model shows that the favorable physical conditions were detected during two periods (Figure 8). The first period corresponds to a long-lived period of "Pre-Main" type mineralization during which a shallow pluton (less than 8 km depth) is able to create PZM during the emplacement period. This "Pre-Main" type mineralization might then correspond to the EHE observed in the W1 north vein system (292 Ma stage in Figure 15 of Marcoux et al., 2015). The second period corresponds to a shorter-lived period of "Main" type mineralization, gathering the stages I (W), II(Au-As-Bi-Te) and II(Zn-Cu) of Marcoux et al. (2015), and relates to the initiation of the cooling period of the

shallow pluton (Figures 8 and 9).

To investigate this time-lag between these two periods of hydrothermal activities; during the emplacement phase of intrusion and the initial cooling phase, the isotopic closure temperatures muscovite and biotite were mapped in the 3D numerical model (Figure 10). The values of 350° and 450°C were used for the closure temperatures of muscovite and biotite, respectively (Spear 1993; Villa 1998). This temperature range is shown by grey regions in Figure 10. The mapping results show clearly that the W1 structure, which hosts PZM during early pluton emplacement (Figure 8) is colder than the Ar^{40}/Ar^{39}closure temperature of biotite at the time of the hottest phase (i.e. 10 Myrs; Figure 10) while the temperature in the granite core is still higher than the closure temperature range. The same temperature range crosses the granite after 0.04 Myr of cooling (Figure 10). Thus, due to advective heat transfer in permeable zones, a time-lag is observed between the emplacement of the intrusives and related proximal high permeability zones (i.e. W1 structure). This result is in accordance with theoretical models of Eldursi et al. (2009), in which the presence of PZM before the hottest phase of the pluton was demonstrated.

In the 3D hydrothermal modeling, this time-lag (ca. 2.8 Myrs) is shorter than the one observed in the field, with the Tighza natural case showing a time-lag of around 5 Myrs, (i.e. 291 Ma to 286 Ma). From the modeling work, it appears that with a longer pluton emplacement time, the time-lag (gap) between “Pre-Main” and “Main” types of mineralization increases because the intruded magma creates warm conditions in which the fronts of closure temperature of muscovite and biotite need a longer time to pass through the W1 vein and then the parent granite. Consequently, the time-lag between the mineralization formed in W1 and the parent granite becomes longer. Although the numerical modeling did not take the chemical and deformation contributions into account, the results show that the time-lag between mineralization and the parent intrusion can be produced by favorable physical conditions for mineralization before the cooling period (crystallization phase). This time-lag

could be as long as the period of magma emplacement.

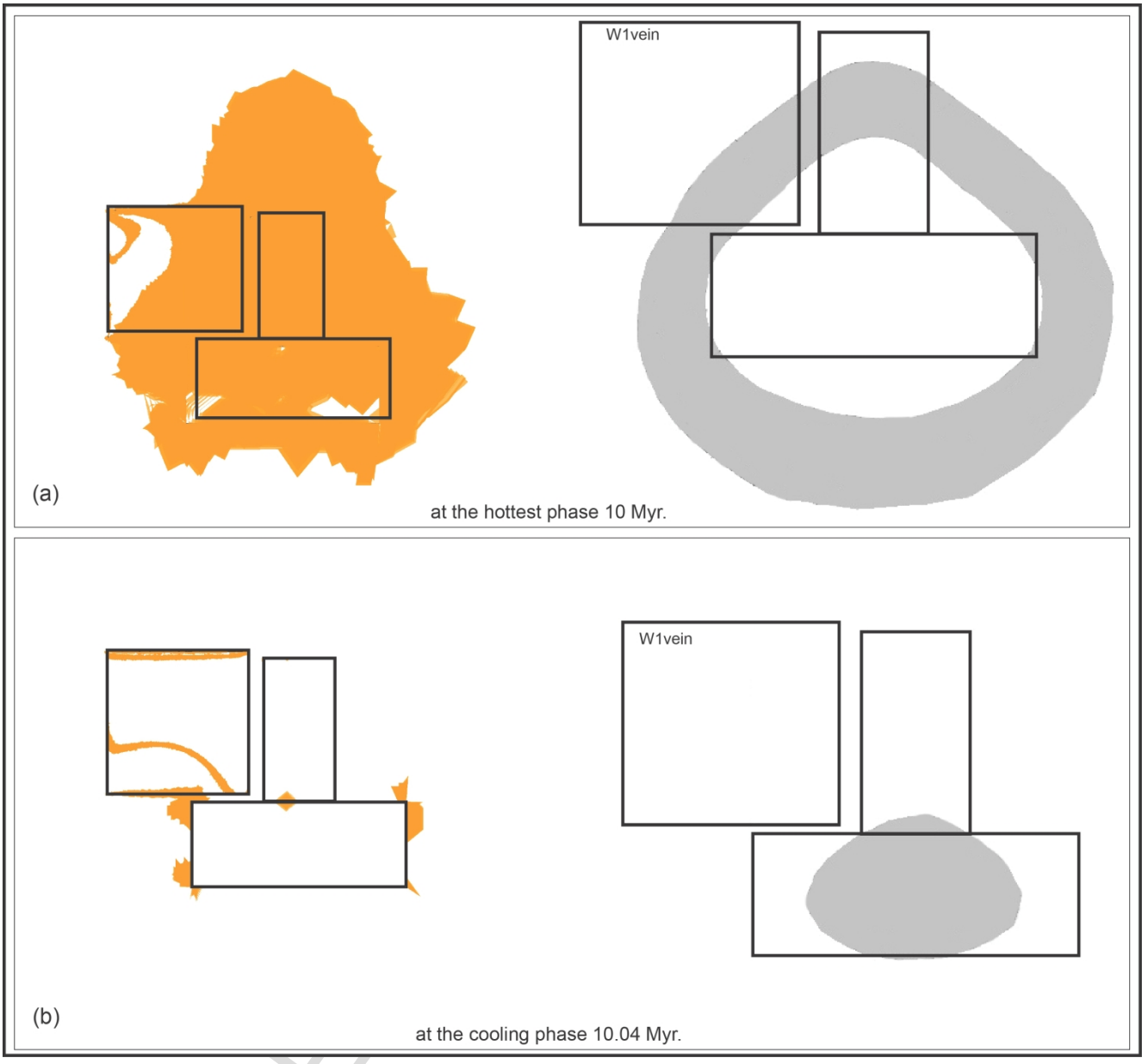

Figure 10 Biotite-Muscovite closure temperatures (the grey zone) cross the permeable zone at the hottest phase (a), and cross the intruded body after 0.04 Myr of cooling (b), the orange zone indicates the R^2AI zone.

6. Conclusion

Based on the geological, petrophysical, and geophysical data, 3D geometrical modeling of the Tighza region suggests that the granitic stocks of the area are connected in the subsurface to a plutonic mass of

batholith-like shape that was rooted in the north at the E-W Tighza fault and that spread toward the south during a D1 extensional regime. The available geophysical data and gravity inversion presented in this work does not allow us to depict the scenario of two hidden plutonic bodies in the subsurface proposed by Cheilltez et al. (2015) and Rossi et al. (2017).

The 3D numerical modeling of thermally-driven fluid flow demonstrated that: 1) suitable physical conditions for mineralization can take place before the crystallization of the parent granite. 2) regardless of whether the W-Au mineralization belongs to "Pre-Main" or "Main" types, the time-lag between early mineralization and young parent magma intrusion could be established to be as long as several hundreds of thousands to millions of years depending on the period of emplacement and/or cooling rate.

Acknowledgments

This work was partly funded by the University of Benghazi (Benghazi, Libya), as it was a part of K. Eldursi thesis. We thank M. Lazaar General Manager of the CMT Mining Company, for free access to the Tighza mine. On the mine site, we are indebted to M. Ouchtouban, T. Montoy, H. Bounajma for field, logistic assistance, and access to mining documents. We extend our sincere gratitude to M. Rossi and an anonymous reviewer for their help to improve the first version of the manuscript. Special thanks to David Quirt (AREVA Resources Canada Inc.) for his constructive remarks and final review of the manuscript.

Appendix

All governing equations, physical laws, boundary conditions, and initial thermal and fluid flow regimes are the same as those published in Eldursi et al. (2009).

1. The physical model

The model geometry for the host rock was a box-like shape with dimensions of 47x40x25 km (Figure 7). The geometry of the Tighza pluton was simplified and drawn based on the final geometrical model produced according to the geological, petrophysical, and geophysical data. The W1 fracture/fault was simulated by a box with dimensions of 0.2x1x1 km. The permeability of the W1 fault follows a depth-dependent equation during the first phase, and is fixed at 10^{-15} m^2 during the second and third phases. The permeability of the host rock follows the Manning and Ingebritsen (1999) depth-permeability curve during the three phases:

$$\log(K) = -14 - 3.2\log(Z) \quad (1)$$

The permeability of the pluton for the first two phases (steady-state and emplacement of magma) follows Manning and Ingebritsen (1999) depth-dependent equation, and is fixed at 10^{-24} m^2 during the third phase (cooling phase).

2. The governing equations and parameters

The thermally-driven fluid flow model for Tighza is governed by different partial differential equations such as Darcy's law, and mass and energy conservations, expressed as, respectively:

$$\vec{u} = -\frac{k}{\mu}\left(\vec{\nabla} p - \rho_L \vec{g}\right) \quad (2)$$

$$\frac{\partial(\Phi \rho_L)}{\partial t} = -\nabla.(\rho_L \overrightarrow{u}) \quad (3)$$

$$Q = C_{eq}\left(\frac{\partial T}{\partial t}\right) + \nabla.\left(-\lambda_{eq}\vec{\nabla} T\right) + C_L \vec{u}\vec{\nabla} T \quad (4)$$

589 The fluid density depends on temperature by the linear approximation.

590 $$\rho_L = \rho_0 (1 - \alpha_v (T - T_0)) \quad (5)$$

591 The fluid dynamic viscosity also varies with temperature (Rabinowicz et al.,1998)

592 $$\mu(T) = 2.414\ 10^{-5} \times \exp\left(\frac{247.8}{T - 140}\right) \quad (6)$$

593 where T is in K and μ is in Pa s.

594 The thermal conductivity, heat capacity, and densities of the host rock and intrusives were also varied
595 with temperature during the three phases, for more details see Eldursi (2009) and Eldursi et al. (2009).

596

597 **3. The boundary and initial conditions**

598 For the thermal part of the modeling, the bottom and upper boundaries were fixed at 700 and 20°C,
599 respectively, whereas the vertical boundaries were set as "thermally insulating". The intruded body
600 was set as a time-dependent heat source at 500 $mW.m^{-3}$ in order to reach 750°C during 3 Ma of
601 emplacement. Then the heat source was turned off when the magma temperature reached 700°C. For
602 the hydraulic part of the modeling, the bottom and vertical boundaries were set as impermeable
603 boundaries; whereas the upper boundary was set as a permeable boundary at a constant pressure of 10^5
604 Pa.. The initial temperature and pressure were governed by the following equations:

605 $$T = 20 + 0.024 * z \quad (7)$$

606 where 0.024 is the geothermal gradient (in °C/m),

607 $$P = P_0 + \rho_L * g * z \quad (A8)$$

608 where P_0 is the atmospheric pressure.

609

610

611

612

613

614

615

616 *Table (1): units and symbols of the used parameters and variables, after Eldursi et al. (2009).*

Parameter	Unit	Symbol
Fluid velocity	$m\ s^{-1}$	u
Permeability	m^2	K
Dynamic viscosity	Pa s	μ
Fluid density	$Kg\ m^{-3}$	ρ_L
Fluid pressure	Pa	p
Gravitational acceleration	$m\ s^{-2}$	g
Depth	m	z
	km	Z
Volumetric coefficient of thermal expansion	K^{-1}	α_v
Weighted average volumetric heat capacity	$J\ m^{-3}\ K^{-1}$	C_{eq}
Specific heat capacity	$J\ kg^{-1}\ K^{-1}$	C_p
Thermal conductivity	$W\ m^{-1}\ K^{-1}$	λ
Equivalent thermal conductivity	$W\ m^{-1}\ K^{-1}$	λ_{eq}
General heat source	$W\ m^{-3}$	Q
Volumetric heat capacity of moving fluid	$J\ m^{-3}\ K^{-1}$	C_L
Temperature	K	T
Porosity, (5% in pluton, host rock and permeable zone)	-	Φ

617

619 **References**

620 Agard, J., Balcon J.M., Morin P. 1958 Etude géologique et métallogénique de la région minéralisée du
621 Jbel Aouam (Maroc central); Notes et Mém. Serv. Géol. Maroc. 126–132.
622 Annen C., Scaillet B., Sparks S.J. 2006 Thermal constraints on the emplacement rate of a large
623 intrusive complex: the Manaslu Leucogranite, Nepal Himalaya. J. Petrol. 47, 71–95.
624 Arboleya M.L., Teixell A., Charroud M., Julivert M. 2004 A structural transect through the High and
625 Middle Atlas of Morocco, J. Afr. Earth Sci. 39, 319–327.
626 Baker T., Lang J.R. 2001 Fluid inclusion characteristics of intrusion-related gold mineralization,
627 Tombstone tungsten magmatic belt, Yukon Territory, Canada. Miner. Deposita. 36, 477–489.
628 Calcagno P., Martelet G., Gumiaux C. 2002 Apport de la modélisation géométrique 3D à
629 l'interprétation géologique du complexe de Champtoceaux (massif armoricain). 19ème RST,
630 Nantes. 79.
631 Calcagno P., Chilès J.P., Courrioux G., Guillen A. 2008 Geological modeling from field data and
632 geological knowledge Part I. Modelling method coupling 3D potential-field interpolation and
633 geological rules. Physics of the Earth & Plan. Interi. 171, 147–157.
634 Carten R.B., Walker B.M., Geraghty E.P., Gunow A.J. 1988 Comparison of field-based studies of the
635 Henderson porphyry molybdenum deposits, Colorado, with experimental and theoretical models of
636 porphyry systems. In Taylor R.P. & Strong D.F. (eds), Recent Advances in the geology of Granite-
637 related Mineral Deposits, 351–66, Spec. Vol.39, Can. Inst. Min. Metall., Montréal.
638 Cheilletz A., Zimmermann J.L. 1982 Datations par la méthode K-Ar du complexe intrusif et des
639 minéralisations en tungstène du jbel Aouam (Maroc central). C.R. Acad. Sc. Paris, t. 295 série II,
640 255–258.
641 Cheilletz, A., 1983. Le contrôle structural des minéralisations filoniennes en tungstène du Djebel
642 Aouam (Maroc Central); application au système filonien. Pb–Zn–Ag. Comptes Rendus Académie

643 des Sciences. Paris, vol. 297, pp. 417–420.
644 Cheilletz A. 1984 Contribution à la géologie du district polymétallique (W-Mo-Cu-Pb-Zn-Ag) du Jbel
645 Aouam, Maroc Central: Thèse de 3ème cycle, I.N.P.L., C.R.P.G., E.N.S.G. Nancy, France p. 250.
646 PhD Thesis.
647 Cheilletz A., Isnard P. 1985 Contribution à la prospection des gisements hydrothermaux de tungstène
648 sur l'exemple du district polymétallique W-Pb-Zn-Ag du jbel Aouam (Maroc central). Miner.
649 deposita 20, pp 220–230 (Extended abstract).
650 Cheilletz A., Rossi M., Tarrieu L., Gasquet D., Bounajma H., Mantoy T., Ouazzani L., Ouchtouban L.,
651 Deloule E., Burnard P., Paquette J. 2015 A Cordilleran Zoning Model for the Polymetallic W-Au-
652 Pb-Zn-Ag Tighza-Jbel Aouam District (Central Morocco): Contribution from New He-Ar and U-
653 Th-Pb Data. 13TH SGA BUENNIAL MEETING. 4, 1579–1582.
654 Desteucq C. 1974 Le système filonien du Jbel Aouam (Maroc Central); essai d'interprétation
655 structurale. Thèse de 3ème cycle Univ. Paul Sabatier Toulouse, France, p. 93. PhD Thesis.
656 Dilles J.H., Profett J.M. 1995 Metallogenesis of the Yerington batholith, Nevada, in: F.W. Pierce, J.G.
657 Bolm (Eds.), Porphyry Copper Deposits of the American Cordillera, American Geological Society
658 Digest 20, pp. 306–315.
659 Eldursi K. 2009 Minéralisations et circulations péri-granitiques: modélisations numérique couplée
660 2D/3D, applications au district minier de Tighza (Maroc central). Thèse de 3ème cycle Univ.
661 Orléans, France, p 218. PhD Thesis.
662 Eldursi K., Branquet Y., Guillou-Frottier L., Marcoux E. 2009 Numerical investigation of transient
663 hydrothermal processes around intrusions: heat transfer and fluid-circulation controlled
664 mineralization patterns. Earth Planet. Sci. Lett. 288, 70–83.
665 Faïk, F., 1988. Le Paléozoïque de la region de Mrirt (Est du Maroc Central) ; évolution stratigraphique
666 et structurale. PhD Thesis, Univ. Paul Sabatier, Toulouse, France.

667 Gerdes M.L., Baumgartner L.P., Person M. 1998 Convective fluid flow through heterogeneous country
668 rocks during contact metamorphism. J. Geophys. Res. 103, 23,983–24,003.
669 Gloaguen E., Branquet Y., Chauvet A., Bouchot V., Barbanson L., Vigneresse J.L. 2014 Tracing the
670 magmatic/hydrothermal transition in regional low-strain zones: The role of magma dynamics in
671 strain localization at pluton roof, implications for intrusion-related gold deposits. J. Struc. Geol. 58,
672 108–121.
673 Guillen A., Calcagno P., Courrioux G., Joly A., Ledru P. 2008 Geological modelling from field data
674 and geological knowledge: Part ii. Modelling validation using gravity and magnetic data inversion.
675 Physics of the Earth & Plan. Interi. 171(1), 158-169.
676 Guillou-Frottier L., Burov E.B., Milési J.P. 2000 Genetic links between ash-flow calderas and
677 associated ore deposits as revealed by large-scale thermo-mechanical modelling. J. Volc. Geotherm.
678 Res. 102, 339–361.
679 Guillou-Frottier L., Burov E.B. 2003 The development and fracturing of plutonic apexes: implications
680 for porphyry ore deposits. Earth Planet. Sci. Lett. 214, 341–356.
681 Harcouët-Menou V., Guillou-Frottier L., Bonneville A., Adler P.M., Mourzenko V. 2009
682 Hydrothermal convection in and around mineralized fault zones: insights from two- and three-
683 dimensional numerical modelling applied to the Ashanti belt, Ghana. Geofluids. 9, 116–137.
684 Hart C.J.R. 2005 Classifying, distinguishing and exploring for intrusion-related gold systems. The
685 Gangue 87, p. 1, 4–9.
686 Hart C.J.R. 2007 Reduced intrusion-related gold systems, in Goodfellow, W.D., ed., Mineral deposits
687 of Canada: A Synthesis of Major Deposit Types, District Metallogeny, the Evolution of Geological
688 Provinces, and Exploration Methods: Geological Association of Canada, Mineral Deposits
689 Division, Special Publication No. 5, 95–112.
690 Joly A., Martelet G., Chen Y., Faure M. 2008 A multidisciplinary study of a syntectonic pluton close

691 to a major lithospheric-scale fault—Relationships between the Montmarault granitic massif and the
692 Sillon Houiller Fault in the Variscan French Massif Central: 2. Gravity, aeromagnetic
693 investigations, and 3-D geologic modeling. J. Geophy. Res. 113, 1–13.
694 Lajaunie C., Courrioux G., Manuel L. 1997 Foliation fields and 3D cartography in geology: Principles
695 of a method based on potential, interpolation, Math. Geol. 29, 571–584.
696 Lang J.R., Baker T. 2001 Intrusion-related gold systems. The present level of understanding. Miner.
697 Deposita 36, 477–489.
698 Lyons J.B., Campbell J.G., Erikson J.P. 1996 Gravity signatures and geometric configurations of some
699 Oliveran plutons: their relation to Acadian structures. Geol. Soci. of Amer. Bull. 108, 872–882.
700 Marcoux É., Nerci K., Branquet Y., Ramboz C., Ruffet G., Peucat J., Stevenson R., Jébrak M. 2015
701 Late-Hercynian intrusion-related gold deposits: An integrated model on the Tighza polymetallic
702 district, central Morocco. J. Afr. Earth Sci. 107, 65–88.
703 Martelet G., Debéglia N. et Truffert C. 2002 Homogénéisation et validation des corrections de terrain
704 gravimétriques jusqu'à la distance de 167km sur l'ensemble de la France, C. R. Geoscience, 334,
705 449–454.
706 Martelet G., Calcagno P., C. Gumiaux C., Truffert C., Bitri A., Gapais D., Brun J.P. 2004 Integrated
707 3D geophysical and geological modelling of the Hercynian Suture Zone in the Champtoceaux area
708 (south Brittany, France). Tectonophy. 382, 117–128.
709 McKenna J.R., Blackwell D.D. 2004 Numerical modeling of transient Basin and Range extensional
710 geothermal systems. Geothermics. 33, 457–476.
711 Nerci K. 2006 Les minéralisations aurifères du district polymétallique de Tighza (Maroc central): un
712 exemple de mise en place périgranitique tardi-hercynienne. Thèse de 3ème cycle Univ. Orléans
713 Orléans, France, p. 210. PhD Thesis.

714 Phillips O.M. 1991 Flow and reactions in permeable rocks. Cambridge University Press, Cambridge.
715 pp. 285.
716 Rabinowicz M., Boulègue J., Genthon P. 1998 Two and three-dimensional modelling of hydrothermal
717 convection in the sedimented Middle Valley segment, Juan de Fuca Ridge. J. Geophy. Res. 103,
718 24045–24065.
719 Raffensperger J.P. and Vlassopoulos D. 1999 The potential for free and mixed convection in
720 sedimentary basins. Hydrogeo. J. 7, 505–520.
721 Ribeyrolles M., 1972 Etude tectonique et microtectonique d'un segment de la chaîne hercynienne dans
722 la partie Sud Orientale du Maroc Central. Thèse de 3ème cycle Univ. Montpellier, Montpellier,
723 France, p. 163. PhD Thesis.
724 Rossi M., Tarrieu L., Cheilletz A., Gasquet D., Deloule E., Paquette J., Bounajma H., Mantoy T.,
725 Ouazzani L., Ouchtouban L. 2016 The Polymetallic (W–Au and Pb–Zn–Ag) Tighza District
726 (Central Morocco): Ages of Magmatic and Hydrothermal Events. Springer, Min. Depo. North Afr.
727 Min. Res. Rev. 107–131.
728 Rossi M., Gasquet D., Cheilletz A., Tarrieu L., Bounajma H., Mantoy T., Reisberg L., Deloule E.,
729 Boulvais P., Burnard P. 2017 Isotopic and geochemical constraints on lead and fluid sources of the
730 Pb-Zn-Ag mineralization in the polymetallic Tighza-Jbel Aouam district (central Morocco), and
731 relationships with the geodynamic context. J. Afr. Earth Sci. 127, 1–17.
732 Seedorff E. 1988 Cyclic development of hydrothermal mineral assemblages related to multiple
733 intrusions at the Henderson porphyry molybdenum deposit, Colorado; Geol. 35, 64–79.
734 Sillitoe R.H. 2000 Gold-rich porphyry deposits: descriptive and genetic models and their role in
735 exploration and discovery. SEG Reviews, 13, 315–345.
736 Spear F. S. 1993 Metamorphic phase equilibria and pressure-temperature-time paths. Miner. Soci. of
737 Amer. p 799.

738 Talbot J.Y., Martelet G., Courrioux G., Chen Y, Faure M. 2004 Emplacement in an extensional setting
739 of the Mont Lozère–Borne granitic complex (SE France) inferred from comprehensive AMS,
740 structural and gravity studies. J. Struc. Geol. 26, 11–28.
741 Tarrieu L. 2014 Nouvelles données minéralogiques, géochimiques et géochronologiques sur le
742 gisement polymétallique de Tighza (Maroc Central) et Contribution à la m métallogénie des
743 gisements de métaux de base filoniens en contexte post-collisionnel. Univ. Savoie, Chambéry,
744 France, p. 240. PhD thesis.
745 Termier H. 1936 Etudes géologiques sur le Maroc central et le Moyen Atlas septentrional. Notes et
746 Mémoires du Service des Mines et de la Carte géologique du Maroc n°33.
747 Thompson J.F.G., Sillitoe R.H., Bake T., Lang J.R., Mortensen J.K. 1999 Intrusion related gold
748 deposits associated with tungsten-tin provinces. Miner. Deposita 34, 323–344.
749 Vigneresse J. L. 1990 Use and misuse of geophysical data to determine the shape at depth of granitic
750 intrusions, Geol. 25, 249–260.
751 Villa I. 1998 Isotopic closure, Terra Nova. 10, 42–47.
752 Wadjinny A. 1998 Le plomb au Maroc: cas des districts de Touissit et de Jbel Aouam. Chronique de la
753 Recherche Minière. 531-532, 9–28.
754 Wallace S.R. 1991 Model development: porphyry molybdenum deposits. Econo. Geol. 8, 207–24.
755 Watanabe Y. 2002.^{40}Ar/^{39}Ar Geochronologic constraints on the timing of massive sulfide and vein-
756 type Pb-Zn mineralization in the Western Meseta of Morocco. Econo. Geol. 97, 145–157.
757 Wei W., Chen Y., Faure M., Martelet G., Lin W., Wang Q., Yan Q., Hou Q. 2016 An early extensional
758 event of the South China Block during the Late Mesozoic recorded by the emplacement of the Late
759 Jurassic syntectonic Hengshan Composite Granitic Massif (Hunan, SE China). Tectonphy. 672–
760 673, 50–67.
761 White D.E. 1981 Active geothermal systems and hydrothermal ore deposits. In Skinner B.J. (eds.),

762 Econo. Geol. 75th Anniv. V. 392–423.

763 Zhao C., Hobbs B.E., Mühlhaus H.B. 1998 Finite element modelling of temperature gradient driven
764 rock alteration and mineralization in porous rock masses. Comput. Meth. Appl. Mech. Eng. 165, 175–
765 187.

Highlights

- Gravity data processing and inversion of Tighza area.
- 3D hydrothermal fluid flow occurred before, during, and after magma emplacement.
- The rock alteration index is useful for detection of the sites of ore deposition.
- “Pre-Main” and “Main” types of ore deposits are associated with magma emplacement.
- Time-lag issues associated with Intrusion-Related Gold Deposits are interpreted.